

## Polyvinyl Alcohol Enhances Acetylation of Ascorbic Acid in Superparamagnetic-Graphene Oxide Nanoparticles Ultrasonically Complexed with Acetylsalicylic Acid

Anastasia Tkach, Uladzimir Fiadosenka, Aliaksandr Burko, Hanna V. Bandarenka, Anna Matsukovich, Nina Krekoten, Ljudmila Tabulina, Vladimir Labunov, and Darya Radziuk

*ACS Appl. Polym. Mater.*, **Just Accepted Manuscript** • DOI: 10.1021/acsapm.0c00648 • Publication Date (Web): 15 Jul 2020

Downloaded from [pubs.acs.org](https://pubs.acs.org) on July 27, 2020

### Just Accepted

“Just Accepted” manuscripts have been peer-reviewed and accepted for publication. They are posted online prior to technical editing, formatting for publication and author proofing. The American Chemical Society provides “Just Accepted” as a service to the research community to expedite the dissemination of scientific material as soon as possible after acceptance. “Just Accepted” manuscripts appear in full in PDF format accompanied by an HTML abstract. “Just Accepted” manuscripts have been fully peer reviewed, but should not be considered the official version of record. They are citable by the Digital Object Identifier (DOI®). “Just Accepted” is an optional service offered to authors. Therefore, the “Just Accepted” Web site may not include all articles that will be published in the journal. After a manuscript is technically edited and formatted, it will be removed from the “Just Accepted” Web site and published as an ASAP article. Note that technical editing may introduce minor changes to the manuscript text and/or graphics which could affect content, and all legal disclaimers and ethical guidelines that apply to the journal pertain. ACS cannot be held responsible for errors or consequences arising from the use of information contained in these “Just Accepted” manuscripts.

1  
2  
3  
4  
5  
6  
7  
8  
9  
10  
11  
12  
13  
14  
15  
16  
17  
18  
19  
20  
21  
22  
23  
24  
25  
26  
27  
28  
29  
30  
31  
32  
33  
34  
35  
36  
37  
38  
39  
40  
41  
42  
43  
44  
45  
46  
47  
48  
49  
50  
51  
52  
53  
54  
55  
56  
57  
58  
59  
60

# Polyvinyl Alcohol Enhances Acetylation of Ascorbic Acid in Superparamagnetic-Graphene Oxide Nanoparticles Ultrasonically Complexed with Acetylsalicylic Acid

*Anastasia Tkach,<sup>1</sup> Uladzimir Fiadosenka,<sup>1</sup> Aliaksandr Burko,<sup>2</sup> Hanna Bandarenka,<sup>2,3</sup> Anna Matsukovich,<sup>4</sup> Nina Krekoten,<sup>5</sup> Ljudmila Tabulina,<sup>1</sup> Vladimir Labunov<sup>1</sup> and Darya Radziuk<sup>1\*</sup>*

<sup>1</sup>Laboratory of Integrated Micro- and Nanosystems, Belarusian State University of Informatics and Radioelectronics, P. Brovki Str. 6, 220013 Minsk, Republic of Belarus

<sup>2</sup>Laboratory of Applied Plasmonics, Belarusian State University of Informatics and Radioelectronics, P. Brovki Str. 6, 220013 Minsk, Republic of Belarus

<sup>3</sup>Polytechnic School, Arizona State University, 6075 S. Innovation Way, Mesa, AZ, 85212, USA

<sup>4</sup>B.I. Stepanov Institute of Physics, National Academy of Sciences, Nezavisimosti Ave. 68, 220072 Minsk, Republic of Belarus

<sup>5</sup>Scientific-Technical Center “Belmicrosystems”, Kazintsa Str. 121 A, 220108 Minsk, Republic of Belarus

KEYWORDS: polymer, graphene, iron oxide, nanoparticle, acetylsalicylic acid.

1  
2  
3 ABSTRACT  
4  
5  
6

7 A single step ultrasonic method (20 kHz) is demonstrated for the formation of acetylsalicylic  
8 acid-Fe<sub>3</sub>O<sub>4</sub>-graphene oxide nanocomposites (~ 80 nm) in aqueous solution. The electronic  
9 molecular structure of these nanocomposites is stable in acidic or basic aqueous medium.  
10  
11 Coating of these nanocomposites with polyvinyl alcohol (PVA) occurs through increased  
12 binding with drug, magnetite, Fe(II)-C-O and carbonaceous network of graphene oxide. PVA-  
13 coated-acetylsalicylic acid-Fe<sub>3</sub>O<sub>4</sub>-GO nanocomposites substantially improve acetylation of  
14  
15 pristine ascorbic acid than free unmodified drug or uncoated acetylsalicylic acid-Fe<sub>3</sub>O<sub>4</sub>-GO  
16  
17 nanoparticles due to enhanced electron density through the presence of magnetite and graphene  
18  
19 oxide, and specific binding of PVA with drug and ascorbic acid.  
20  
21  
22  
23  
24  
25  
26  
27  
28  
29  
30  
31  
32  
33  
34  
35  
36  
37  
38  
39  
40  
41  
42  
43  
44  
45  
46  
47  
48  
49  
50  
51  
52  
53  
54  
55  
56  
57  
58  
59  
60

## 1. Introduction

Acetylsalicylic acid (ASA) is one of the frequently used nonsteroidal anti-inflammatory drugs (NSAIDs) due to its ability not only to reduce fever and kill the pain, but also to prevent cardiovascular disorders<sup>[1]</sup> and improve the survival rate after the breast or colon cancer.<sup>[2,3]</sup> ASA has the unique capacity of acetylating various proteins, hormones, DNA, platelets and hemoglobin, which at least partly explains its wide-ranging pharmacological actions.<sup>[4]</sup> The pharmacological function of ASA is not completely understood, but can be explained by its inhibition of cyclooxygenase (COX) enzymes that block certain prostaglandins synthesis resulting in reduction of pain, fever and inflammation. ASA forms an ionic bond via its carboxyl or enolic group and acts as one of the strongest inhibitors of COX-1 with much less activity against COX-2, and causes the most damage to the stomach.<sup>[5]</sup> The recommended dose of ASA for adults to reach the desired analgesic effect is one tablet every 4-6 hours for several days, and to reach the anti-inflammatory effect is about 3 tablets for 4-6 times a day up to 30 tablets daily. A frequency of the ASA administration at such a high dose will unavoidably cause the gastrointestinal tract injury and many other side effects including symptoms such as gas, bloating, and diarrhea, and allergic reactions. Therefore new approaches are necessary for the healthier administration of ASA by reducing its dose and enhancing its pharmaceutical actions.

The pharmacological property of ASA is based on dynamic conformational changes for covalent modification of the COX protein enabling its oxygenation.<sup>[6]</sup> ASA-treated COX-2 forms polyhydroxylated lipids that exhibit anti-inflammatory activity and can be beneficial for clinical studies. The presence of the carboxylate group affects the charge-charge interaction between ASA and the COX-domain. Conformational changes observed in various NSAID structures have time-dependent inhibition of COX that may occur by more than one mechanism involving

1  
2  
3 electron or oxygen transfer reactions. Probably for this reason, a large number of NSAIDs can be  
4  
5 activated by metal ions resulting in enhanced biological functions including suppression of early  
6  
7 cancer relapse and retardation of tumor growth that, in many cases, are inaccessible to pristine  
8  
9 NSAIDs.<sup>[7]</sup> In general, the anti-inflammatory,<sup>[8]</sup> analgesic,<sup>[9]</sup> antibacterial<sup>[10]</sup> and anti-  
10  
11 proliferative<sup>[11]</sup> progression of metal-NSAID complexes rely on their modified chemical  
12  
13 structure, i.e. coordination of hydrophilic (carboxylic acid, enols) and lipophilic (aromatic ring,  
14  
15 halogen atoms) groups to metal ions. This type of coordination between the metal ion and the  
16  
17 NSAID groups determines their interaction with many intracellular components, resulting in the  
18  
19 desired cell cure or apoptosis.  
20  
21  
22  
23

24 Iron metallodrugs are biologically active compounds that constitute a class of approved  
25  
26 human or veterinary supplements with improved antitumoral, antimalarial, antifungal and  
27  
28 antibacterial activities.<sup>[12]</sup> At the cellular level the capture of iron ions in biologically useful form  
29  
30 occurs through specific complexation with hemoproteins, heme or nonheme enzymes involving  
31  
32 electron transfer in oxidation-reduction reactions. The iron ion absorption can be controlled by  
33  
34 pH via formation of insoluble ferrous  $\text{Fe}^{3+}$  and bioavailable ferric  $\text{Fe}^{2+}$  forms. At low pH, when  
35  
36 an iron ion absorption is reduced, the presence of ascorbate and citrate molecular groups can act  
37  
38 as weak chelators of metal ions, thereby increasing their bioavailability.<sup>[13,14]</sup> Complexation of a  
39  
40 ferric  $\text{Fe}^{2+}$  with ASA significantly improves the selective inhibition of COX, stimulating the  
41  
42 production and secretion of mucus, increasing mucosal blood flow and promoting epithelial cell  
43  
44 proliferation.<sup>[15]</sup> However, small concentration of such compounds, difficulty in the control of  
45  
46 their intact electronic molecular structure and fate *in vivo* substantially limit their application.  
47  
48  
49  
50

51 This limitation can be overcome by developing new methods in nanomedicine to produce  
52  
53 nanoscale compounds with predictable function through the design of their morphology and  
54  
55  
56  
57  
58  
59  
60

1  
2  
3 electronic molecular structure.<sup>[16,17]</sup> Morphology and structure of Fe<sub>3</sub>O<sub>4</sub> nanoparticles can be  
4 controlled by stoichiometry of Fe<sup>3+</sup> and Fe<sup>2+</sup> in aqueous medium via classical hydrothermal<sup>[18,19]</sup>  
5 or modified sonochemical<sup>[20]</sup> routes in conjunction with graphene oxide (GO).<sup>[21,22]</sup> One of the  
6 keys to successful application of such compounds in biomedicine and *in vivo* is the regulation of  
7 their toxicity and structure-function property with biomolecules over biocompatible coating.  
8 Various hydrophilic polymers (e.g. polyethylene glycol,<sup>[23]</sup> polyvinyl alcohol,<sup>[24]</sup> polyaniline,<sup>[25]</sup>  
9 Pluronic F-127,<sup>[26]</sup> poly (D, L-lactide-co-glycolide),<sup>[27]</sup> polycyano-acrylate<sup>[28]</sup>) can be used for  
10 such a coating of magnetic nanocomposites reducing aggregation states, improving  
11 biocompatibility and stability of morphology, and substantially enhancing their distribution in  
12 tissues, cell membrane penetration, intravenous delivery, metabolic clearance and magnetic  
13 targeting of nanoparticles *in vivo*. In contrast to nanoparticles, additional parameters such as the  
14 number of layers, dimension, and carbon-to-oxygen atomic ratio modulate the toxicity of GO.<sup>[29]</sup>  
15 GO is biodegradable because it can be digested by peroxidases naturally present in cells and its  
16 reduced bioaccumulation in cells (tissues) can limit the long-term cytotoxicity.<sup>[30]</sup> Coating of GO  
17 by polyvinyl alcohol (PVA) can significantly reduce the cytotoxicity.<sup>[31]</sup>

18  
19  
20  
21  
22  
23  
24  
25  
26  
27  
28  
29  
30  
31  
32  
33  
34  
35  
36  
37  
38 In our study, we develop a new single step ultrasonic method for the complexation of pristine  
39 ASA with synthesized Fe<sub>3</sub>O<sub>4</sub>-GO nanoparticles and coating the final product with PVA in  
40 aqueous medium. In this study polymer PVA is chosen for coating because it has a carbon  
41 backbone enriched with hydroxyl groups that can substantially enhance the hydrophilicity of  
42 produced ASA-Fe<sub>3</sub>O<sub>4</sub>-GO nanocomposites, improving biocompatibility and dispersion required  
43 for biological application. Our work aims at fundamental investigation of acetylation (main  
44 function of ASA) of ascorbic acid (AA) as a model system by using ASA- Fe<sub>3</sub>O<sub>4</sub>-GO  
45 nanocomposites coated with PVA and disclose the role of this polymer in this reaction.  
46  
47  
48  
49  
50  
51  
52  
53  
54  
55  
56  
57  
58  
59  
60

## 2. Experimental Section

**Materials and Synthesis.** Graphite (~30  $\mu\text{m}$  dispersion) with elemental composition: C ( $95.0 \pm 2.0$  atom.%), O ( $4.0 \pm 1.0$  atom.%), Ti ( $0.1 \pm 0.0$  atom.%), Ca ( $1.1 \pm 0.1$  atom.%).  $\text{H}_3\text{PO}_4$ ,  $\text{KMnO}_4$ ,  $\text{H}_2\text{SO}_4$ ,  $\text{H}_2\text{O}_2$  (60%),  $\text{HCl}$  (35%),  $\text{HNO}_3$  (40%),  $\text{KOH}$  (44%),  $\text{NaOH}$ ,  $\text{C}_2\text{H}_5\text{OH}$ ,  $\text{C}_3\text{H}_8\text{O}$ ,  $\text{FeCl}_3 \cdot 6 \text{H}_2\text{O}$ ,  $\text{FeCl}_2 \cdot 4 \text{H}_2\text{O}$  are of higher grade purity 99% being obtained from Belreachim JSC (Republic of Belarus). Deionized water (DI;  $\text{pH} = 5.5$ , specific conductivity  $5 \mu\text{S} \cdot \text{cm}^{-1}$ ) was prepared by using a homemade distillation apparatus (Republic of Belarus). We synthesized graphene oxide (GO) using the improved Hummers method<sup>[32]</sup> and applied centrifugation (8.59 g) for multiple rinsing, at first, with DI water ( $\text{pH} = 5.5$ ) for a total duration of 90 min and, at second, with a mixture of {DI water : isopropanol} at a volume ratio 1:3 for a total duration of 60 min (more details are in supporting information). The final GO product was obtained after drying at  $100^\circ\text{C}$  in the air. Pristine NSAID – acetylsalicylic acid (ASA) (500 mg) was purchased from Belmedpreparaty RUE (Minsk, Republic of Belarus). Fine powder of ASA was produced by grinding of 10 tablets by using agate mortar and pestle. The aqueous solution of ASA was prepared by dissolving a powder of this drug in DI water ( $\text{pH} = 5.5$ ) under continuous stirring at a critical concentration of dissolution at room temperature according to literature.<sup>[33]</sup> For experiments both NSAID aqueous solutions were filtered through a cellulose membrane filter (red line, the pore size 8-12 nm).

### *a) Sonochemical formation of graphene oxide- $\text{Fe}_3\text{O}_4$ nanoparticles*

A homemade horn-type ultrasonic disperser N.4-20 designed by y Cavitation Inc. (Republic of Belarus) and operating in a continuous mode at 20 kHz frequency with the 400 W maximal output power was used for the sonochemical synthesis of nanoparticles. The ultrasonic intensity of this device was calibrated by using a method of calorimetry.<sup>[34]</sup> Prior to the synthesis of

1  
2  
3 nanocomposites 0.18 g of GO was exfoliated in 10 mL of DI water (DI) (pH = 5.5) by using  
4 ultrasound (10 W/cm<sup>2</sup>) for 30 min in ice-cooled vessel. The exfoliated GO was triply rinsed with  
5  
6 DI water centrifuged at 7.27 g for 45 min, the supernatant was removed and the precipitant was  
7  
8 added by aqueous solution of 44% KOH (pH = 12).  
9

10  
11  
12 In a vessel of 30 mL H<sub>2</sub>O a mixture of {0.86 g FeCl<sub>2</sub> + 2.35 g FeCl<sub>3</sub>} was heated to 80°C in  
13  
14 an Ar atmosphere under vigorous stirring for 15 min. Soon after 5 mL 44 % KOH was dropwise  
15  
16 added into this heated mixture and the suspension became black. This black solution was heated  
17  
18 at 80°C for an additional 30 min under continuous stirring, added by the exfoliated GO (0.14 g of  
19  
20 preformed GO was added by 4 mL H<sub>2</sub>O and sonicated under stirring until the homogeneous  
21  
22 solution was obtained) and sonicated at 18 W/cm<sup>2</sup> for 90 min. This sonochemical synthesis was  
23  
24 carried out in a sealed reaction vessel coated by a lid connected to an Ar tube and placed in the  
25  
26 ice bath in order to control low temperature. Then the colloidal solution was triply rinsed with DI  
27  
28 water at 6.71 g for 30 min and dried at 100°C to obtain a powder. Formed nanocomposites could  
29  
30 be easily dispersed in an aqueous solution and collected by an external permanent magnet.  
31  
32  
33

34  
35 *b) Sonochemical coating of graphene oxide-Fe<sub>3</sub>O<sub>4</sub> nanoparticles with polyvinyl alcohol*

36  
37 Aqueous solution of PVA was prepared by dissolving 0.022 g of polymer in 10 mL of DI  
38  
39 water under stirring in an open air for 30 min. Then it was added by 100 mg of graphene oxide-  
40  
41 Fe<sub>3</sub>O<sub>4</sub> nanoparticles (powder) and sonicated for 15 min (15 W/cm<sup>2</sup>) in an open air in ice-cooled  
42  
43 vessel. The final product was triply rinsed by centrifugation at 8.12 g for 15 min and dried at  
44  
45 100°C. This procedure was applied for the coating of preformed Fe<sub>3</sub>O<sub>4</sub> nanoparticles.  
46  
47  
48

49  
50 *c) Ultrasonic functionalization of pristine ASA with graphene oxide-Fe<sub>3</sub>O<sub>4</sub> and graphene*  
51  
52 *oxide-Fe<sub>3</sub>O<sub>4</sub>-PVA nanoparticles*  
53  
54  
55  
56  
57  
58  
59  
60



1  
2  
3 Powder of GO-Fe<sub>3</sub>O<sub>4</sub> nanoparticles was mixed with the fine powder of pristine ASA at  
4 equimolar concentration and ultrasonically treated (18 W/cm<sup>2</sup>) in 30 mL of DI water (pH = 5.5)  
5 for 5 min in an air in an ice-cooled vessel. Final colloidal suspension was triply rinsed with DI  
6 water at 8.12 g for 15 min and dried at 100°C to obtain a powder. Formed nanocomposites could  
7 be easily dispersed in aqueous solution and collected by an external permanent magnet.  
8  
9

10  
11  
12 30 mL of aqueous solution of ASA (1.67 mg/mL) was added by graphene oxide-Fe<sub>3</sub>O<sub>4</sub>-PVA  
13 nanoparticles (10 mg) and sonicated for 5 min (18 W/cm<sup>2</sup>) in an open air in an ice-cooled vessel.  
14 Final products were triply washed by centrifugation (at 8.12 g) for 15 min and dried at 100°C to  
15 obtain a powder. Control experiments were performed by treating each of graphene oxide  
16 powder or Fe<sub>3</sub>O<sub>4</sub> nanoparticles and the powder of pristine ASA at equimolar concentration with  
17 ultrasound (18 W/cm<sup>2</sup>) followed by the thorough rinsing with DI water. This procedure was  
18 applied for the ultrasonic functionalization of ASA with preformed Fe<sub>3</sub>O<sub>4</sub>-PVA nanoparticles.  
19  
20  
21  
22  
23  
24  
25  
26  
27  
28  
29

30  
31 *d) Acetylation of pristine ascorbic acid by graphene oxide-Fe<sub>3</sub>O<sub>4</sub>-ASA and graphene oxide-*  
32 *Fe<sub>3</sub>O<sub>4</sub>-PVA-ASA nanocomposites*  
33  
34

35 30 mL of aqueous solution of ascorbic acid (1.67 mg/mL) was added by 10 mg of graphene-  
36 Fe<sub>3</sub>O<sub>4</sub>-ASA or graphene-Fe<sub>3</sub>O<sub>4</sub>-PVA coated-ASA nanocomposites under thermal stirring for  
37 60 min in an air. The temperature of the reaction solution was not allowed to exceed 80°C. After  
38 reaction colloidal suspensions were cooled down to room temperature and triply rinsed with DI  
39 water by using centrifugation (6.71 g).  
40  
41  
42  
43  
44  
45  
46

47 **Equipment and Analytical Methods.** The synthesized nanomaterials were characterized  
48 through several methods: Dynamic Light scattering (DLS), Zeta Potential (ZP), scanning  
49 electron microscopy (SEM) and energy dispersive X-ray fluorescence (EDX), X-ray powder  
50 diffraction (XRD), confocal Raman and SERS spectroscopy, UV-visible absorption and Fourier-  
51  
52  
53  
54  
55  
56  
57  
58  
59  
60

1  
2  
3 transform infrared spectroscopy. The size distribution and  $\xi$ -potential of colloids were measured  
4  
5 by DLS from Malvern Instruments Ltd. by using a Zetasizer Nano instrument and a prepared  
6  
7 buffer solution.<sup>[35]</sup> DLS and  $\xi$ -potential (electrical charge) experiments were carried out on a 50  
8  
9 times diluted colloidal suspension. Each measurement took 10 s; the nanoparticle distribution  
10  
11 and electrophoretic curves were obtained by averaging ten measurements. The morphology and  
12  
13 elemental composition of sonochemically prepared nanomaterials were analyzed and  
14  
15 characterized by SEM (S-4800) Hitachi, Japan. The phase composition was determined by using  
16  
17 powder diffraction patterns recorded with an EMPYREAN diffractometer (PANalytical,  
18  
19 Netherlands) using Cu-K $\alpha$  radiation (Ni-filter) at 296 K.  
20  
21  
22  
23

24 Raman and SERS spectra were recorded by using a 3D scanning laser confocal Raman  
25  
26 microscope Confotec NR500 (SOL Instruments Ltd., Republic of Belarus) at 633 nm excitation  
27  
28 wavelength with a grating 600gr/mm blazed at 600 nm. The Si wafer with the characteristic  
29  
30 Raman line at 520 cm<sup>-1</sup> was taken as a reference for calibration and basic alignment during  
31  
32 integration time from 1 to 3 s. The SERS-measurements were performed with the silvered porous  
33  
34 silicon (Ag/PS) substrates described elsewhere<sup>[36]</sup> in order to enhance Raman signals of  
35  
36 molecular compounds. The SERS-active substrates were kept in each freshly prepared aqueous  
37  
38 colloidal solution for 2 hours and then taken out of glass vessels. Immediately afterwards  
39  
40 incubated SERS-active substrates were rinsed with DI water and air-dried. The acquired Raman  
41  
42 and SERS spectra were corrected for the baseline and a background of the SERS-active  
43  
44 substrates based on Ag/PS. A linearly polarized diode laser beam was focused through the  
45  
46 objectives with 40x and 100x magnification for Raman and SERS spectra acquisition. The laser  
47  
48 power (4 mW) was attenuated by using neutral density filters with the following optical density  
49  
50 (OD) values 0.6 (25), 0.3 (50) and no filter (100).  
51  
52  
53  
54  
55  
56  
57  
58  
59  
60

The crystallite size of carbonaceous nanostructures  $L_a$  (nm) was calculated by using the following equation<sup>[37]</sup> (1)

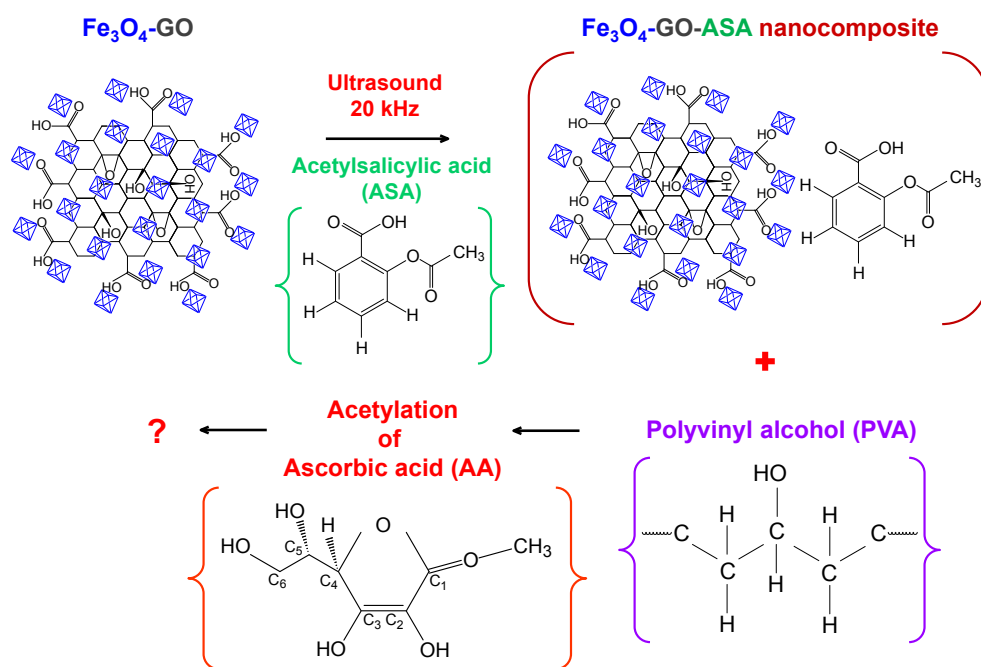
$$L_a = \frac{(2.4 \cdot 10^{-10}) \lambda_{laser}^4}{Int_D / Int_G}, \quad (1)$$

where  $L_a$  – the crystallite size of carbonaceous nanostructures (nm),  $\lambda_{laser}$  – the excitation laser wavelength (nm),  $Int_D / Int_G$  – the intensity ratio of Raman D and G lines.

The UV-visible absorption spectra of colloidal solutions were recorded by using a Cary-500 spectrophotometer (Varian, USA) in the wavelength range from 200 to 800 nm. The molecular structure of nanocomposites was revealed by FTIR Vertex 70 Bruker spectrometer (Germany) in the range from 400 to 4000  $cm^{-1}$  by using Zeiss Jena Specord-75IR (Germany).

### 3. Results and Discussion

The main idea of the present work is illustrated in **Scheme 1**.



**Scheme 1.** Synthesized graphene oxide-Fe<sub>3</sub>O<sub>4</sub> nanoparticles are used for the ultrasonic functionalization of pristine ASA (20 kHz, 18 W/cm<sup>2</sup>) resulting in the formation of graphene oxide-Fe<sub>3</sub>O<sub>4</sub>-ASA nanocomposite as a final product. This product was ultrasonically coated with PVA in order to perform acetylation of pristine AA in aqueous solution.

In this work two goals are pursued: 1) sonochemical functionalization of pristine ASA with preformed graphene oxide-Fe<sub>3</sub>O<sub>4</sub> nanoparticles (Fe<sub>3</sub>O<sub>4</sub>-GO) and 2) study of acetylation of pristine AA (AA) with graphene oxide-Fe<sub>3</sub>O<sub>4</sub>-ASA nanocomposites (Fe<sub>3</sub>O<sub>4</sub>-GO-ASA) coated with PVA and revealing the role of PVA in this reaction.

### 3.1 Morphology and composition of Fe<sub>3</sub>O<sub>4</sub>-GO nanoparticles

The sonochemically formed graphene oxide-Fe<sub>3</sub>O<sub>4</sub> nanoparticles can be collected by the external permanent magnet in aqueous solution showing the magnetic nature of this material (**Figure 1A**). These nanoparticles have irregular cubic morphology with the mean size of 78 ± 9 nm (**Figure 1B and C**). **Figure 1D** shows SERS spectra of synthesized graphene oxide-Fe<sub>3</sub>O<sub>4</sub> nanoparticles (red line) in comparison with pristine graphene oxide (black line). SERS spectrum of GO shows two peaks that can be assigned to K-point phonons of A<sub>1g</sub> D breathing mode (~ 1340 cm<sup>-1</sup>) and zone center phonons of E<sub>2g</sub> G mode (~ 1603 cm<sup>-1</sup>) with their intensity ratio Int<sub>D</sub>/Int<sub>G</sub> ~ 1.17, indicating that synthesized GO consists of mixture of amorphous and crystalline regions containing carbon with sp<sup>2</sup> hybridization.<sup>[38]</sup> The intensity of disorder-induced D mode is relatively low (~ 0.42) pointing out to a structural perfection of a carbon material.<sup>[39]</sup> The Full Width at Half Maximum (FWHM) of G mode (~ 57 cm<sup>-1</sup>) is smaller than of D mode (~ 90 cm<sup>-1</sup>), demonstrating relatively low structural disorder of GO that contains localized sp<sup>2</sup> dimers or shorter sp<sup>2</sup> chains with a sharper length distribution.<sup>[40]</sup> The crystallite size of GO is ~ 32.92 nm according to eq. (1). The surface structure of GO was examined by FTIR absorption

1  
2  
3 spectroscopy (Figure S1, Supporting Information). FTIR spectrum of GO shows strong  
4 vibrational bands of C-O at  $\sim 1103\text{ cm}^{-1}$ ,  $\nu(\text{COO})$  in  $\text{COO}^-$  at  $\sim 1459\text{ cm}^{-1}$ , aromatic and  
5 unsaturated bands  $\nu(\text{COO})$  in  $(\text{HCOO}^-)$  of carboxylic group at  $\sim 1570\text{ cm}^{-1}$ , C=C at  $\sim 1628\text{ cm}^{-1}$ , -  
6 C=O of carboxylic group at  $\sim 1743\text{ cm}^{-1}$ , asymmetric and symmetric C-H stretching vibrations at  
7  $\sim 2854\text{ cm}^{-1}$  and  $\sim 2927\text{ cm}^{-1}$ , and O-H stretching band at  $\sim 3433\text{ cm}^{-1}$ ,<sup>[41]</sup> demonstrating that  
8 oxidation process during the synthesis of GO resulted in the formation of hydroxyl and  
9 carboxylic groups with the presence of aromatic regions, typical for oxidized graphene  
10 nanoribbons.<sup>[42]</sup> However, the surface of synthesized GO doesn't contain epoxide groups because  
11 the characteristic C-O bands at  $1220\text{-}1225\text{ cm}^{-1}$  are absent. The presence of carboxyl and  
12 hydroxyl groups on the surface of synthesized GO with aromatic regions points out that GO  
13 retains its functionality with enhanced electronic properties, which can be used for more efficient  
14 acetylation of ascorbic acid.

15  
16  
17  
18  
19  
20  
21  
22  
23  
24  
25  
26  
27  
28  
29  
30  
31 In contrast, SERS spectrum of  $\text{Fe}_3\text{O}_4$ -GO nanoparticles shows multiple peaks that can be  
32 assigned to Fe(II)-CO ( $\sim 480$  and  $525\text{ cm}^{-1}$ ),<sup>[41]</sup>  $\text{Fe}_3\text{O}_4$  ( $\sim 554$ ,  $626$  and  $660\text{ cm}^{-1}$ ),<sup>[43]</sup>  $\gamma\text{-Fe}_2\text{O}_3$   
33 ( $\sim 725$  and  $765\text{ cm}^{-1}$ ),<sup>[44]</sup> epoxide group of GO ( $\sim 853\text{ cm}^{-1}$ ),<sup>[45]</sup> Fe-O ( $\sim 1038\text{ cm}^{-1}$ ),<sup>[46]</sup>  $\text{FeCO}_3$   
34 ( $\sim 1080\text{ cm}^{-1}$ )<sup>[47]</sup> (**Figure 1D**, red line). Vibrational bands at  $\sim 1160$  and  $1425\text{-}1465\text{ cm}^{-1}$  can be  
35 assigned to GO that correspond to nanocrystalline diamond as a result of the sum and difference  
36 modes of C-C with  $\text{sp}^2$  hybridization and C-H vibrations of transpolyacetylene type segments  
37 occurring at grain boundaries.<sup>[48]</sup> The presence of H-ending C=C chain was observed at  
38  $\sim 1160\text{ cm}^{-1}$  and aromatic carbonate at  $\sim 1221\text{ cm}^{-1}$ .<sup>[49]</sup>

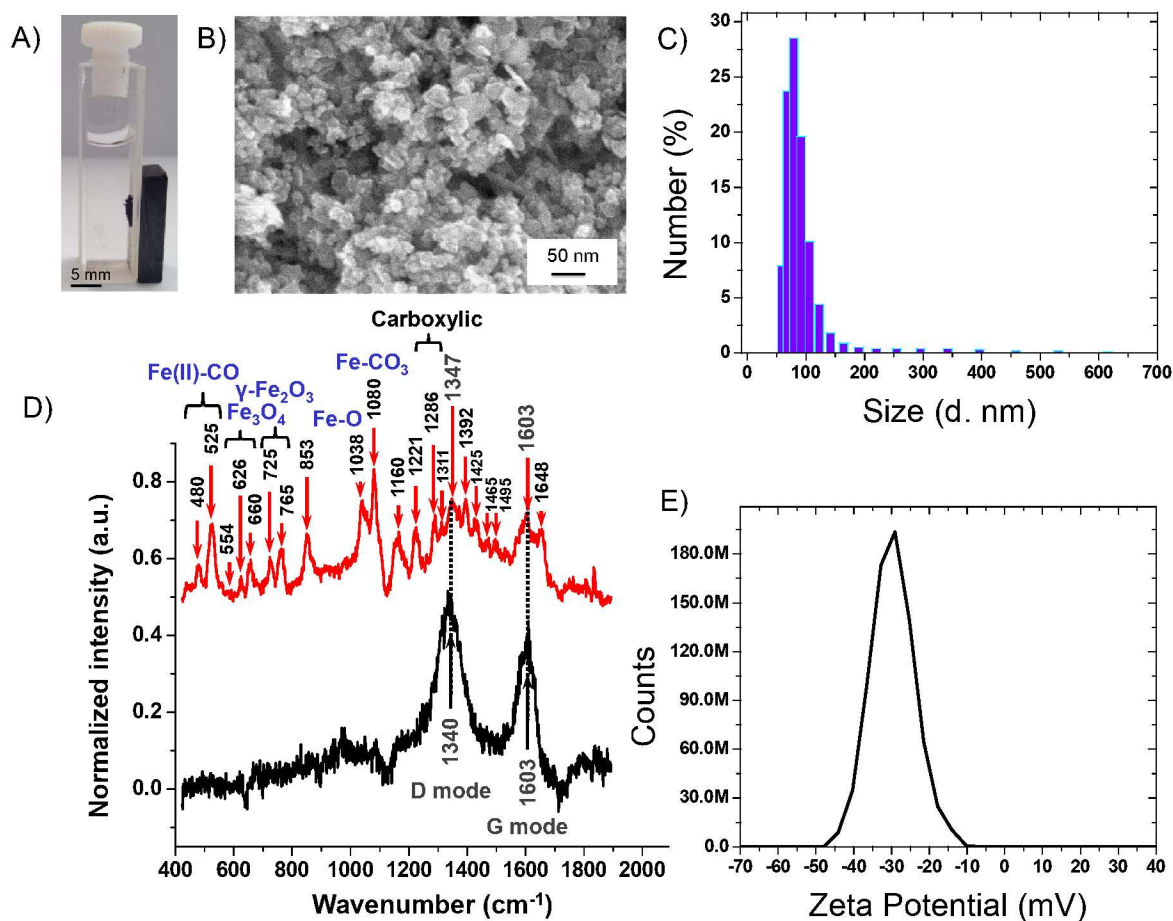


**Figure 1.** A) True color photo image of sonochemically synthesized graphene oxide-Fe<sub>3</sub>O<sub>4</sub> nanoparticles that can be collected by an external permanent magnet. B) Representative SEM image and C) DLS size distribution diagram showing morphology of these nanoparticles of < 100 nm. D) SERS spectra of synthesized graphene oxide (black line) and sonochemically formed graphene oxide-Fe<sub>3</sub>O<sub>4</sub> nanoparticles (red line). E) Zeta potential plot of prepared graphene oxide-Fe<sub>3</sub>O<sub>4</sub> nanoparticles demonstrating the negative surface charge.

Carboxylic acid groups can be revealed by their characteristic Raman peaks at 1286 and 1311 cm<sup>-1</sup> in the nanocomposite. The D mode is shifted at ~ 1347 cm<sup>-1</sup> and the G mode (~ 1603 cm<sup>-1</sup>) developed a shoulder at 1648 cm<sup>-1</sup>, demonstrating the changes of the dimensions

1  
2  
3 and structural ordering of the layers that can be caused by the formation of Fe<sub>3</sub>O<sub>4</sub>-GO  
4 nanocomposite.<sup>[50]</sup> The intensity ratio Int<sub>D</sub>/Int<sub>G</sub> is ~ 0.82, demonstrating the lower total number  
5 of defects that are present in nanocomposite than in GO. The calculated FWHM values of D and  
6 G lines are smaller in Fe<sub>3</sub>O<sub>4</sub>-GO than in GO and the G peak (~ 33 cm<sup>-1</sup>) is broader than the D  
7 peak (~ 20 cm<sup>-1</sup>), pointing out that the formation of nanocomposite did not destroy the chemical  
8 bonds of graphene and didn't break its structure. The crystallite size of Fe<sub>3</sub>O<sub>4</sub>-GO nanocomposite  
9 is ~ 47.27 nm, which is larger than that of GO. This small peak at 1648 cm<sup>-1</sup> can arise from non-  
10 regular rings in a C divacancy.<sup>[51]</sup>

11  
12  
13  
14  
15  
16  
17  
18  
19  
20  
21  
22  
23  
24  
25  
26  
27  
28  
29  
30  
31  
32  
33  
34  
35  
36  
37  
38  
39  
40  
41  
42  
43  
44  
45  
46  
47  
48  
49  
50  
51  
52  
53  
54  
55  
56  
57  
58  
59  
60  
The Zeta potential of Fe<sub>3</sub>O<sub>4</sub>-GO nanocomposites is -29.9 ± 6.3 mV (**Figure 1E**) due to the  
presence of O (49.6 ± 4.1 at.%), C (26.9 ± 1.9 at.%) and Fe (20.4 ± 1.4 at.%) as revealed from  
the EDS analysis (**Figure S2** and **Table S1**).

### 3.2 Crystalline and electronic molecular structure of Fe<sub>3</sub>O<sub>4</sub>-GO nanoparticles

The phase composition and crystalline structure of Fe<sub>3</sub>O<sub>4</sub>-GO nanocomposites were revealed  
from X-Ray powder diffraction patterns (**Figure 2A**) and the experimental data were compared  
with synthesized GO (**Table 1** and **2**). The XRD diagram of graphene oxide shows an elevated  
continuum with several small peaks at 2θ = 12.24 and 38.36 arising from GO,<sup>[52]</sup> 34.95 and 40.12  
indicating the presence of diamond phase and 42.71 due to graphite phase that is in agreement  
with the crystallographic database of diamond (amcsd 0013983) and graphite (amcsd 0000049)  
(**Figure 2A** and **Table 1**).

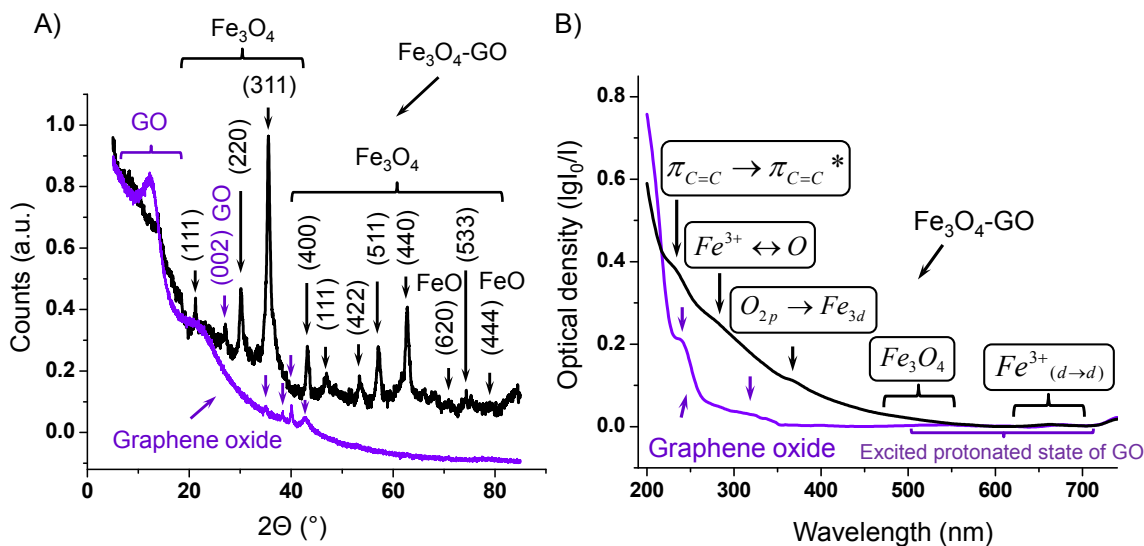


**Figure 2.** A) X-Ray powder diffraction patterns and B) UV-visible absorption spectra of synthesized graphene oxide (GO) and sonochemically formed Fe<sub>3</sub>O<sub>4</sub>-GO nanoparticles.

A broad small peak of at  $2\theta = 12.24$  points out to the heterogeneous structure of GO containing graphite domains with  $sp^2$  and  $sp^3$  hybridization.<sup>[53]</sup>

**Table 1.** X-Ray powder diffraction data of synthesized graphene oxide (GO).

$2\theta, ^\circ$	I, a.u.	(hkl)	$d_{hkl}, \text{\AA}$	Material (Phase)
12.24	8	(001)	7.07	GO
34.95	1	(020)	2.56	GO (diamond)
38.36	1	-	2.35	GO
40.12	2	(021)	2.27	GO (diamond)
42.71	1	(020)	2.12	GO (graphite)

The XRD pattern of sonochemically synthesized Fe<sub>3</sub>O<sub>4</sub>-GO nanoparticles shows characteristic reflexes of Fe<sub>3</sub>O<sub>4</sub> crystalline phase (amcsd 0020645) with changed  $d$  interplanar spacing values due to the effect of pressure gradient (Table 2). The calculated  $d$  values point out



to the effect of pressure gradient from  $\sim 1$  atm ( $\approx 10^{-4}$  GPa) to  $\sim 1\text{-}20 \cdot 10^3$  atm ( $< 2$  GPa) that can be produced in cavitation hot spots.<sup>[54]</sup> The XRD diagram reveals the presence of FeO (amcsd 0013895) and a possible recoverable high-pressure and high-temperature polymorph of iron oxide  $\text{Fe}_4\text{O}_5$  (amcsd 0018509).<sup>[55]</sup>  $\text{Fe}_4\text{O}_5$  can be produced upon heating at 1500-2200 K as a result of a breakdown of magnetite into one of iron oxide phases depending on the pressure gradient. The recently discovered phase  $\text{Fe}_4\text{O}_5$  can result from the breakdown of magnetite into  $\text{Fe}_4\text{O}_5$  and  $\text{Fe}_2\text{O}_3$ . However, the XRD pattern of  $\text{Fe}_3\text{O}_4$ -GO nanoparticles shows only reflexes of  $\text{Fe}_3\text{O}_4$  and FeO phases. Therefore the presence of high pressure  $\text{Fe}_4\text{O}_5$  phase is less probable.

**Table 2.** X-Ray powder diffraction data of sonochemically formed  $\text{Fe}_3\text{O}_4$ -GO nanoparticles.

$2\theta, ^\circ$	I, a.u.	(hkl)	$d_{\text{hkl}}, \text{\AA}$	Material (Phase)
8.08	9	-	11.61	GO
13.92	19	-	6.53	GO
18.38	11	(111)	4.82	$\text{Fe}_3\text{O}_4$
21.26	15	(001)	4.10	GO (diamond)
27.07	13	(002)	3.33	GO (graphite)
30.18	30	(220)	2.96	$\text{Fe}_3\text{O}_4$
35.51	100	(311)	2.53	$\text{Fe}_3\text{O}_4$
43.20	23	(400)	2.09	$\text{Fe}_3\text{O}_4$
46.96	11	(111)	1.92	GO (graphite)
48.46	7	(112)	1.85	GO (diamond)
51.53	5	(220)	1.78	GO (diamond)
53.36	13	(422)	1.72	$\text{Fe}_3\text{O}_4$
57.13	26	(511)	1.61	$\text{Fe}_3\text{O}_4$
62.73	41	(440)	1.48	$\text{Fe}_3\text{O}_4$

66.19	8	(222)	1.40	GO (diamond)
68.27	9	(132)	1.36	GO (diamond)
70.90	7	(620)	1.33	FeO
74.44	11	(533)	1.27	Fe <sub>3</sub> O <sub>4</sub>
78.73	6	(444)	1.21	FeO

As next, we examined the electronic molecular structure of Fe<sub>3</sub>O<sub>4</sub>-GO nanoparticles by using UV-visible absorption spectroscopy (**Figure 2B**). The absorption spectrum of GO exhibits two bands: at ~236 nm (5.28 eV) arising from the  $\pi$ - $\pi^*$  transition of aromatic C=C bonds and ~320 nm (3.88 eV) as a result of the n- $\pi^*$  transition of C=O bonds. In contrast, the UV-visible absorption spectrum of Fe<sub>3</sub>O<sub>4</sub>-GO nanoparticles is manifold with bands on elevated continuum that can be assigned to the  $\pi_{c=c} \rightarrow \pi_{c=c}^*$  transition in GO comparable to graphene quantum dots;<sup>[56]</sup> Fe<sup>3+</sup> ↔ O (4.31 eV), <sup>6</sup>A<sub>1</sub> → <sup>4</sup>T<sub>1</sub>(4p) (4.12 eV) and O<sub>2p</sub> → Fe<sub>3d</sub> (3.41 eV, isosbestic point of Fe<sub>3</sub>O<sub>4</sub> nanoparticles) as a result of the enhanced electronic conjugation of graphene,<sup>[57]</sup> the intervalence charge transfer between Fe<sup>3+</sup> and O existing in magnetite nanocrystals and Fe-O bonds in the carbonaceous network of GO<sup>[58]</sup> and Fe<sup>3+</sup>(d → d) (1.79 eV) in conjunction with the excited protonated state of GO.

### 3.3 Ultrasonic complexation of ASA with Fe<sub>3</sub>O<sub>4</sub>-GO nanoparticles

Synthesized Fe<sub>3</sub>O<sub>4</sub>-GO nanoparticles were used for ultrasonic complexation with pristine ASA resulting in formation of ASA-Fe<sub>3</sub>O<sub>4</sub>-GO nanoparticles. The UV-visible absorption spectroscopy was used to find out how ASA is complexed with Fe<sub>3</sub>O<sub>4</sub>-GO nanoparticles and what is the role of GO and magnetite in this process (**Figure 3**).

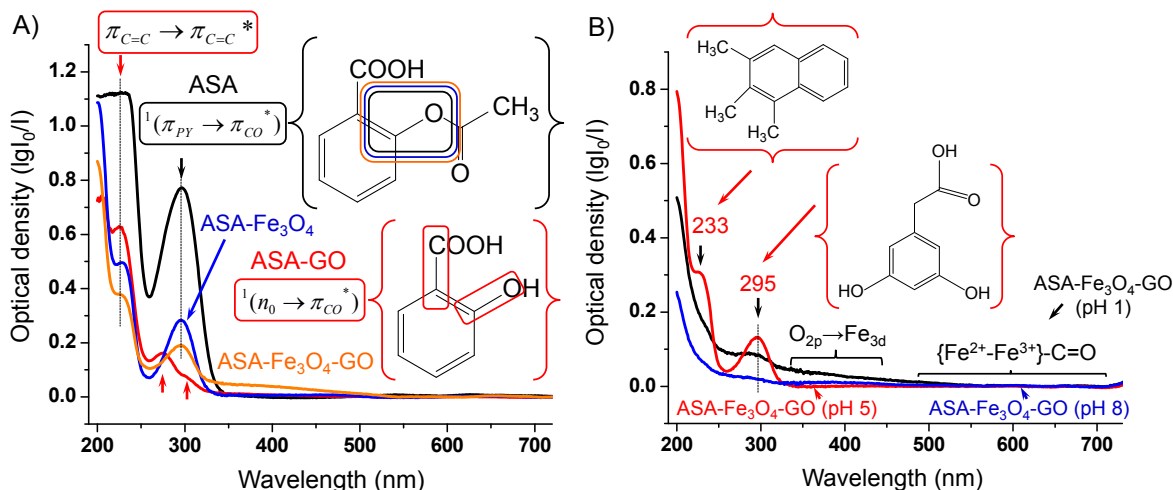


**Figure 3.** UV-visible absorption spectra of A) pristine ASA (black line), ASA-Fe<sub>3</sub>O<sub>4</sub>-GO nanoparticles (orange line) in comparison with ASA-GO (red line) and ASA-Fe<sub>3</sub>O<sub>4</sub> (blue line) after sonication (20 kHz, 18 W/cm<sup>2</sup>) in aqueous solution and B) ASA-Fe<sub>3</sub>O<sub>4</sub>-GO nanoparticles after aging in DI water at pH 1, 5 or 8.

UV-visible absorption spectrum of ASA-Fe<sub>3</sub>O<sub>4</sub>-GO nanoparticles in aqueous solution exhibits two bands: at 226 nm ( $\sim 5.49$  eV) due to the  $\pi_{C=C} \rightarrow \pi_{C=C}^*$  transition in GO and 295 nm ( $\sim 4.20$  eV) arising from the  $^1(\pi_{py} \rightarrow \pi_{co}^*)$  transition of the  $\pi$  (bonding) molecular orbital from the phenyl ring in  $-C=C-$  or  $C=O$  to its  $\pi^*$  (anti-bonding) orbital in the ASA<sup>[59]</sup> and  $^1(n_o \rightarrow \pi_{co}^*)$  transition in  $C=C$  or  $C=O$  of the carboxylic groups in salicylic acid<sup>[60]</sup> (**Figure 3A**). For comparison, aqueous solution of pristine ASA exhibits strong absorption band in the region from  $\sim 200$ -250 nm and characteristic peak at  $\sim 296$  nm that is indicative of ASA functional groups.<sup>[61]</sup> The first broad band overlaps with the characteristic absorbance of pristine GO ( $\sim 236$  nm). ASA-Fe<sub>3</sub>O<sub>4</sub> nanoparticles in aqueous solution exhibit absorption bands similar to ASA-Fe<sub>3</sub>O<sub>4</sub>-GO with GO peak being red shifted at  $\sim 228$  nm ( $\sim 5.44$  eV) that can be caused by the changes of the methyl group in ASA. In contrast, UV-visible absorption spectrum of ASA-GO

nanoparticles shows two bands: at 277 nm (ASA) and 302 nm (salicylic acid). The OD values of ASA band in all types of nanoparticles vary from highest to lowest in the following order: pristine ASA  $\rightarrow$  ASA-Fe<sub>3</sub>O<sub>4</sub>  $\rightarrow$  ASA-Fe<sub>3</sub>O<sub>4</sub>-GO  $\rightarrow$  ASA-GO (**Table 3**). The ratio OD (pristine ASA)/OD (type of ASA nanoparticle) is the highest in ASA-GO and the lowest in ASA-Fe<sub>3</sub>O<sub>4</sub>, pointing out to the difference in the binding affinity of ASA to GO and magnetite components and their catalytic activity in the Fe<sub>3</sub>O<sub>4</sub>-GO structure. Magnetite may enhance the electronic density of ASA in ASA-Fe<sub>3</sub>O<sub>4</sub>-GO nanocomposite and GO may control the electron charge transfer of ASA and accelerate the acetylation.

**Table 3.** UV-visible absorption data of pristine ASA, ASA-Fe<sub>3</sub>O<sub>4</sub>, ASA-GO and ASA-Fe<sub>3</sub>O<sub>4</sub>-GO nanoparticles in aqueous solution.

Compound	Peak, nm	Optical density (lgI <sub>0</sub> /I), a.u.	Ratio*, a.u.
<i>pristine ASA</i>	296	0.77	1
ASA-GO	277 and 302	0.17 and 0.08	4.53 and 9.63
ASA-Fe <sub>3</sub> O <sub>4</sub>	295	0.29	2.66
ASA-Fe <sub>3</sub> O <sub>4</sub> -GO	295	0.20	3.91
<i>pristine GO</i>	236	1.12	1
ASA-GO	227	0.64	1.75
ASA-Fe <sub>3</sub> O <sub>4</sub>	228	0.50	2.25
ASA-Fe <sub>3</sub> O <sub>4</sub> -GO	226	0.38	2.95

\*Ratio is calculated by dividing the optical density (OD) value of pristine ASA or GO (in italic) with the OD magnitudes of ASA-GO, ASA-Fe<sub>3</sub>O<sub>4</sub> and ASA-Fe<sub>3</sub>O<sub>4</sub>-GO.

The stability of ultrasonically formed ASA-Fe<sub>3</sub>O<sub>4</sub>-GO nanoparticles was examined by aging aqueous colloidal solutions adjusted at pH 1, 5 or 8 and recording UV-visible absorption spectra (**Figure 3B**). After the treatment the most intense absorbance of ASA-Fe<sub>3</sub>O<sub>4</sub>-GO nanoparticles was observed at pH 5 with the appearance of bands at ~233 nm (characteristic of ASA with

naphthalene-trimethyl structure) and 295 nm. These bands became smoothed on elevated absorption continuum at pH 1 and almost vanished at pH 8. At pH 1 the broadening of the characteristic ASA peak at 295 nm was accompanied with an absorbance near 400 nm and 600 nm, demonstrating the presence of dihydroxyphenyl acetic acid structure of the salicylic acid because of its complexation with ferrous ions that can be formed as reaction products of  $\text{Fe}_3\text{O}_4$  dissolution in acidified water.<sup>[61]</sup> Heating during acoustic cavitation may favor the solubilization of salicylic acid in water with intramolecular H-bonding capable of protolytic dissociation, i.e. exchange in the intramolecular proton movements in the salicylic acid and its specific binding to  $\text{Fe}_3\text{O}_4$ -GO because of the excited multiple  $\text{O}_{2p} \rightarrow \text{Fe}_{3d}$  and  $\{\text{Fe}^{2+}-\text{Fe}^{3+}\} @ \text{C}=\text{O}$  transitions. The contribution of  $\text{O}_{2p} \rightarrow \text{Fe}_{3d}$  transitions and H-bonding in ASA- $\text{Fe}_3\text{O}_4$ -GO structure is negligible at pH 5, but not at pH 8 because absorbed water molecules have a specific effect on the stability of the ASA- $\text{Fe}_3\text{O}_4$  complex in a basic aqueous medium. Quantum chemical calculations reveal that the dimer with two H-bonds can be more stable through two carboxyl groups via the charge transfer and electrostatic interaction,<sup>[63]</sup> in agreement with the absorption bands in the 200-300 nm spectral range. This is because the  $n$  electrons of anions of organic acids in the GO structure are highly affected by the H-bond formation. The energy levels of  $n$  electrons decrease significantly in water and this causes a shift in an absorption maximum of an  $n \rightarrow \pi^*$  transition, which is almost equal to the energy of the formed H-bond. The decreased intensity of the peak at 295 nm indicates the expanded polarity of water as a consequence of the increased solvation of  $n$  electrons.

### 3.4 Effect of PVA on acetylation of ascorbic acid by ASA- $\text{Fe}_3\text{O}_4$ -GO nanocomposites

As next, the ability of sonochemically formed ASA- $\text{Fe}_3\text{O}_4$ -GO nanoparticles to acetylate AA was examined by SERS spectroscopy in comparison with ASA- $\text{Fe}_3\text{O}_4$ -GO-PVA and pristine AA

1  
2  
3 being thermally treated with ASA in order to reveal the role of PVA in this reaction (**Figure 4**).  
4  
5 The detailed assignment of vibrational bands of thermally treated pristine AA, AA acetylated by  
6  
7 ASA-Fe<sub>3</sub>O<sub>4</sub>-GO and ASA-Fe<sub>3</sub>O<sub>4</sub>-GO-PVA nanoparticles can be found in the Supporting  
8  
9 Information (**Table S2**). SERS spectra are shown in the region 250-1000 cm<sup>-1</sup> (**Figure 4A**) and  
10  
11 900-2000 cm<sup>-1</sup> (**Figure 4B**). SERS spectra of AA acetylated with ASA-Fe<sub>3</sub>O<sub>4</sub>-GO or ASA-  
12  
13 Fe<sub>3</sub>O<sub>4</sub>-GO-PVA nanoparticles didn't reveal any bands in the region 2000-3500 cm<sup>-1</sup>, therefore  
14  
15 they are not shown. For comparison, we also performed Raman and SERS measurements and  
16  
17 spectral analysis of free pristine AA (**Figure S3** and **Table S3**), ASA (**Figure S4** and **Table S4**)  
18  
19 and PVA (**Figure S5** and **Table S5**). Control experiments were performed by thermal treating of  
20  
21 and PVA (**Figure S5** and **Table S5**). Control experiments were performed by thermal treating of  
22  
23 ASA-Fe<sub>3</sub>O<sub>4</sub>-GO and ASA-Fe<sub>3</sub>O<sub>4</sub>-GO-PVA without AA (more details about spectral analysis can  
24  
25 be found in the Supporting Information, **Figure S6** and **S7**, **Table S6** and **S7**), and of pristine AA  
26  
27 without nanoparticles (**Figure S8** and **Table S8**).  
28  
29

30  
31 The SERS spectrum of pristine AA thermally treated with ASA shows most of characteristic  
32  
33 bands of AA<sup>[64]</sup> (Figure S3 and Table S3) with several shifted peaks at ~ 448 cm<sup>-1</sup> (OH wagging  
34  
35 of AA\**a* and  $\delta_A(\text{OCOCH}_3) + \gamma_A(\text{CC})_{\text{rings}}$  of ASA),<sup>[65]</sup> ~ 1042 cm<sup>-1</sup> (C<sub>1</sub>-O<sub>4</sub>, C<sub>3</sub>-C<sub>4</sub>, C<sub>6</sub>-O<sub>6</sub>  
36  
37 stretching of AA and  $\delta_s(\text{CH})_{\text{rings}}$  of ASA), ~ 1195 cm<sup>-1</sup> (C-O-H bending of AA and  $\nu_{\text{as}}(\text{O-CO-}$   
38  
39 CH<sub>3</sub>) +  $\delta_{\text{as}}(\text{CH}_3)$  of ASA) and ~ 1367 cm<sup>-1</sup> (C<sub>1</sub>-C<sub>2</sub>, C<sub>3</sub>-C<sub>4</sub> stretching and ring OH bending of AA  
40  
41 and  $\delta_{\text{ss}}(\text{CH}_3)$  of ASA), demonstrating acetylation of ascorbic by ASA. Two Raman bands of AA  
42  
43 that appear without shift at 423 cm<sup>-1</sup> and 1607 cm<sup>-1</sup> can be assigned to {C<sub>6</sub>-O<sub>6</sub> torsion of AA and  
44  
45  $\delta_A(\text{O-CO-CH}_3)_{\text{sciss}} + \gamma_A(\text{CC})_{\text{rings}}$  of ASA} and { C<sub>1</sub>-O<sub>1</sub>, C<sub>2</sub>-C<sub>3</sub>, C<sub>2</sub>-O<sub>2</sub> stretching of AA and  
46  
47  $\nu_s(\text{CC})_{\text{rings}}$  of ASA} due to binding of AA with ASA.  
48  
49

50  
51 SERS spectrum of ASA-Fe<sub>3</sub>O<sub>4</sub>-GO-ascorbic acid nanoparticles shows characteristic bands of  
52  
53 ascorbic acid (Figure S3 and Table S3), magnetite at ~ 671 cm<sup>-1</sup> with  $\gamma$ -Fe<sub>2</sub>O<sub>3</sub> phase (~ 763 cm<sup>-1</sup>  
54  
55  
56  
57  
58  
59  
60

1  
2  
3 <sup>1</sup>), Fe-C-O ( $\sim 1080\text{ cm}^{-1}$ ) and Fe-C ( $\sim 1338\text{ cm}^{-1}$ ) along with  $A_{1g}$  D mode and  $E_{2g}$  G mode of  
4 graphene oxide ( $\sim 1582\text{ cm}^{-1}$ ) of graphene oxide, indicating the strong binding of AA with  
5 magnetite within carbonaceous network of graphene (Figure 4 and Table S2). Raman bands: at  
6  $\sim 1190\text{ cm}^{-1}$  that is assigned to {C-C(-O)-O stretching AA and  $\nu_{as}(\text{O-CO-CH}_3) + \delta_{as}(\text{CH}_3)$  of  
7 ASA},  $\sim 1363\text{ cm}^{-1}$  to {  $C_1$ - $C_2$ ,  $C_3$ - $C_4$  stretching and ring OH bend. of AA,  $\delta_{ss}(\text{CH}_3)$  of ASA}  
8 and  $\sim 1461\text{ cm}^{-1}$  to { C-H bending of AA and  $\delta_s(\text{OH}) + \delta_{as}(\text{CH}_3) + \delta_s(\text{CH})_{\text{rings}}$  of ASA}  
9 demonstrate the binding of methyl groups of ASA to AA.  
10  
11  
12  
13  
14  
15  
16  
17  
18

19 SERS spectrum of ASA- $\text{Fe}_3\text{O}_4$ -GO-PVA-ascorbic acid nanoparticles reveals several bands of  
20 pristine AA and AA along with characteristic peaks of Fe(II)-CO and CO of PVA ( $\sim 488\text{ cm}^{-1}$ ),  
21 CO of AA with Fe(II)-CO ( $\sim 572\text{ cm}^{-1}$ ), magnetite ( $\sim 676\text{ cm}^{-1}$ ) with  $\gamma$ - $\text{Fe}_2\text{O}_3$  phase and ring  
22 deformation of AA ( $\sim 729\text{ cm}^{-1}$  and  $\sim 766\text{ cm}^{-1}$ ) and  $C_4$  bending of AA with  $\gamma(\text{CH}_2)$  of PVA  
23 ( $\sim 823\text{ cm}^{-1}$ ), demonstrating that binding of PVA with AA occurs involving Fe-C-O and  
24 magnetite. Raman  $A_{1g}$  D mode of GO is shifted at  $\sim 1327\text{ cm}^{-1}$  with Fe-C and a peak of  $E_{2g}$  G  
25 mode remains ( $\sim 1581\text{ cm}^{-1}$ ) in the polymer matrix due to the appearance of several PVA  
26 vibrational bands. In contrast to ASA- $\text{Fe}_3\text{O}_4$ -GO-ascorbic acid nanoparticles (without PVA), this  
27 nanocomposite exhibits more Raman bands: at  $\sim 423\text{ cm}^{-1}$  that is assigned to { $C_6$ - $O_6$  torsion of  
28 AA and  $\delta_s(\text{O-CO-CH}_3) + \gamma_s(\text{C-C})$  of ASA},  $\sim 448\text{ cm}^{-1}$  to {OH wagging of AA\* and  $\delta_s(\text{O-CO-}$   
29  $\text{CH}_3) + \gamma_s(\text{C-C})$  of ASA},  $\sim 901$ - $943\text{ cm}^{-1}$  to { $\delta_s(\text{CC})$  rings +  $\delta_s(\text{O-CO-CH}_3)$  of ASA},  $\sim 1008$ -  
30  $1013\text{ cm}^{-1}$  to {(O-CO- $\text{CH}_3) + \text{CH}_3$  of ASA},  $\sim 1191$ - $1208\text{ cm}^{-1}$  to {(C-H) AA,  $\nu_{as}(\text{O-CO-CH}_3) +$   
31  $\delta_{as}(\text{CH}_3)$  ASA,  $\nu_s(\text{CC} + \text{CO})$  PVA},  $\sim 1220\text{ cm}^{-1}$  to { $\nu_s(\text{Ph-O-CO-CH}_3) + \delta_s(\text{CH})_{\text{rings}}$  of ASA}  
32 and  $\sim 1370\text{ cm}^{-1}$  to { $C_1$ - $C_2$ ,  $C_3$ - $C_4$  stretching and ring OH bend. of AA,  $\delta_{ss}(\text{CH}_3)$  of ASA},  
33 pointing out to the more effective acetylation of AA by ASA in the presence of PVA and  
34 magnetite bonded to GO.  
35  
36  
37  
38  
39  
40  
41  
42  
43  
44  
45  
46  
47  
48  
49  
50  
51  
52  
53  
54  
55  
56  
57  
58  
59  
60

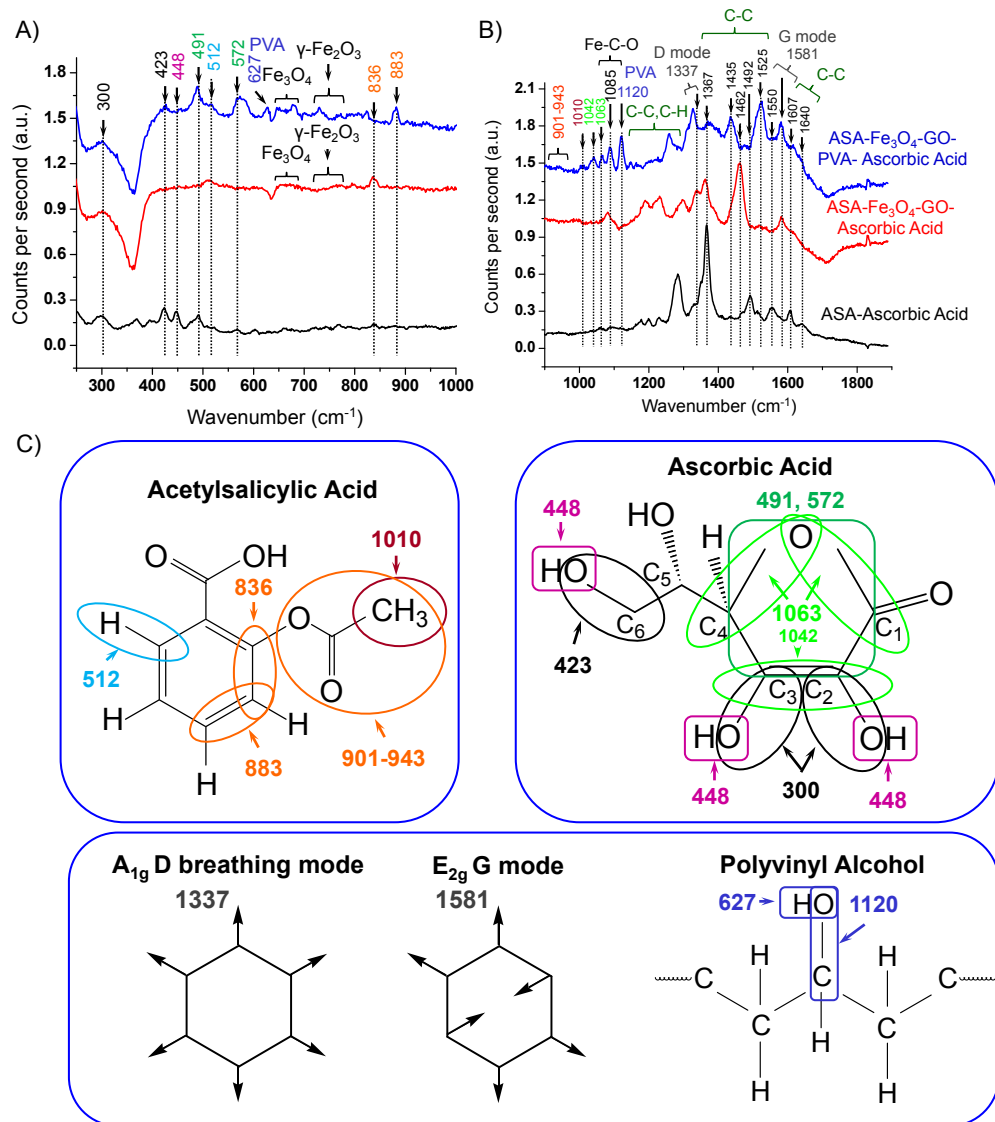


**Figure 4.** A) and B) SERS spectra of pristine ascorbic acid after thermal treating with ASA at  $T \approx 80^\circ\text{C}$  (black line) and ascorbic acid acetylated by ASA-Fe<sub>3</sub>O<sub>4</sub>-GO (red line) and ASA-Fe<sub>3</sub>O<sub>4</sub>-GO-PVA (blue line) nanocomposites ( $\lambda_{\text{exc}} = 633 \text{ nm}$ ) after thermal stirring at  $T \approx 80^\circ\text{C}$  for 60 min. C) Schematic illustration of chemical structures of ASA, ascorbic acid and PVA with defined Raman chemical vibrational bonds obtained from spectra.

In addition, several distinct Raman bands at  $\sim 627 \text{ cm}^{-1}$  (C<sub>4</sub>-C<sub>5</sub> stretching and ring deformation of AA and  $\gamma(\text{OH})$  of PVA<sup>[66]</sup>),  $\sim 823 \text{ cm}^{-1}$  (C<sub>4</sub> on plane bending of AA and  $\gamma(\text{CH}_2)$



1  
2  
3 of PVA) that are assigned to AA with PVA; and  $\sim 646 \text{ cm}^{-1}$  ( $\delta_s(\text{CC})_{\text{rings}} + \delta_s(\text{O-C=O}) +$   
4  $\delta_s(\text{COOH})$  of ASA and  $\gamma(\text{OH})_{\text{twist}}$  of PVA),  $\sim 1147 \text{ cm}^{-1}$  ( $\delta_s(\text{CH})_{\text{rings}}$  of ASA and  $\nu_s(\text{CC} + \text{CO})$  of  
5 PVA) and  $\sim 1435 \text{ cm}^{-1}$  ( $\delta_{\text{as}}(\text{CH}_3)$  of ASA,  $\delta(\text{CH}_2)$  of PVA) that are assigned to ASA with PVA  
6 demonstrate that PVA enhances specific interaction with AA and also ASA.  
7  
8  
9  
10  
11

#### 12 **4. Conclusions**

13  
14  
15 A new ultrasonic single step method (20 kHz) was demonstrated for the formation of ASA-  
16  $\text{Fe}_3\text{O}_4$ -graphene oxide nanocomposites ( $78 \pm 9 \text{ nm}$ ) in aqueous solution. These  
17 superparamagnetic nanoparticles have a stable electronic molecular structure with increased  
18 electron density due to the specific binding of magnetite with GO. ASA- $\text{Fe}_3\text{O}_4$ -GO  
19 nanocomposites exhibit more efficient acetylation of AA in comparison with free pristine ASA.  
20 Coating of these nanocomposites with PVA significantly enhances acetylation of pristine AA  
21 (AA) due to the stronger binding of polymer to ASA, AA, magnetite and GO involving Fe(II)-C-  
22 O. This new knowledge substantially refines our understanding about the improvement of  
23 pharmaceutical function of ASA and discloses the important role of biocompatible polymer, iron  
24 oxide and graphene oxide nanoparticles in it.  
25  
26  
27  
28  
29  
30  
31  
32  
33  
34  
35  
36  
37  
38  
39  
40  
41  
42  
43  
44  
45  
46  
47  
48  
49  
50  
51  
52  
53  
54  
55  
56  
57  
58  
59  
60

### Supporting Information.

The following files are available free of charge.

Synthesis of GO; FTIR absorption spectrum of GO; Energy Dispersive X-Ray fluorescence spectra of synthesized Fe<sub>3</sub>O<sub>4</sub>-GO nanoparticles; SERS spectra and analysis of pristine ascorbic acid with ASA, ascorbic acid with ASA-Fe<sub>3</sub>O<sub>4</sub>-GO or ASA-Fe<sub>3</sub>O<sub>4</sub>-GO-PVA nanocomposites after thermal stirring at T ≈ 80°C for 60 min; Raman and SERS spectra and analysis of aqueous solutions of free unmodified ascorbic acid, ASA and PVA; Raman spectra of thermally treated (T ≈ 80°C for 60 min) ASA-Fe<sub>3</sub>O<sub>4</sub>-GO and ASA-Fe<sub>3</sub>O<sub>4</sub>-GO-PVA nanoparticles (without ascorbic acid).

### Corresponding Author

\*Darya Radziuk, E-mail: [radziuk@bsuir.by](mailto:radziuk@bsuir.by)

### Author Contributions

The manuscript was written through contributions of all authors. All authors have given approval to the final version of the manuscript.

### Funding Sources

This work is supported by the BRFFR grant № 16-3041 57 031.00 and MOST Belarus-EU financial program through grants № R-YPQZ-53145 and 57111R-dDMu-57100.

### Acknowledgment

Prof. Mikhail Artemyev and Prof. Ludmila Ivashkevich from the Belarusian State University (Minsk) are gratefully acknowledged for the ZP/DLS, XRD measurements and constructive discussions.

1  
2  
3  
4  
5  
6  
7  
8  
9  
10  
11  
12  
13  
14  
15  
16  
17  
18  
19  
20  
21  
22  
23  
24  
25  
26  
27  
28  
29  
30  
31  
32  
33  
34  
35  
36  
37  
38  
39  
40  
41  
42  
43  
44  
45  
46  
47  
48  
49  
50  
51  
52  
53  
54  
55  
56  
57  
58  
59  
60

## References

1. Patrono, C.; Baigent, C. Role of aspirin in primary prevention of cardiovascular disease. *Nat. Rev. Cardiol.*, **2019**, *16*, 675-686.
2. Chen, W. Y.; Holmes, M. D. Role of aspirin in breast cancer survival. *Curr. Oncol. Rep.*, **2017**, *19*, 1-48.
3. Patrignani, P.; Patrono, C. Aspirin and cancer. *JACC*, 2016, *68*, 967-976.
4. Alfonso, L.; Ai, G.; Spitale, R. C.; Bhat, G. J. Molecular targets of aspirin and cancer prevention. *Brit. J Cancer*, **2014**, *111*, 1-7.
5. Jane, V. Towards a better aspirin. *Nature*, **1994**, *367*, 215-216.
6. Rouzer, C. A.; Marnett, L. J. Cyclooxygenases: structural and functional insights. *J Lipid Res.*, **2009**, *50*, S29-S34.
7. Banti, C. N.; Hadjidakou, S. K. *Eur. J. Inorg. Chem.*, **2016**, *2016*, 3048-3071.
8. Metal ions on biological systems. Ed. A. Sigel and H. Sigel, Volume 41: Metal ions and their complexes in medication. 2004, CRC Press, 600 p.
9. Leung, C.-H.; Lin, S.; Zhong, H.-J.; Ma, D.-L. Metal complexes as potential modulators of inflammatory and autoimmune responses. *Chem. Sci.*, **2015**, *6*, 871-884.
10. Sun, Y.; Heidary, D. K.; Zhang, Z.; Richards, C. I.; Glazer, E. C. Bacterial cytological profiling reveals the mechanism of action of anticancer metal complexes. *Mol. Pharmaceutics*, **2018**, *15*, 3404-3416.
11. Banti, C. N.; Papatriantafyllopoulou, C.; Tasiopoulos, A. J.; Hadjidakou, S. K. New metalo-therapeutics of NSAIDs against human breast cancer cells. *Eur. J Med Chem.*, **2018**, *143*, 1687-1701.
12. Vitorino, H. A.; Mantovanelli, L.; Zanotto, F. P.; Espósito, B. P. Iron metallodrugs: stability, redox activity and toxicity against artemia salina. *PLoS ONE* **2015**, *10*, e0121997.
13. Crichton R., Iron metabolism: from molecular mechanisms to clinical consequences, 4<sup>th</sup> Ed., Chapter 2: The essential role of iron in biology. John Wiley & Sons, Ltd., 2016, p. 556.
14. Abbaspour, N.; Hurrell, R.; Kelishadi, R. Review on iron and its importance for human health. *J Res. Med. Sci.*, **2014**, *19*, 164-174.
15. Iqbal, M. S.; Khurshid, S. J.; Muhammad, B. Anti-inflammatory and selective COX-2 inhibitory activities of metal complexes of Schiff bases derived from aldoses. *Med. Chem. Res.*, **2013**, *22*, 861-868.
16. Wu, Y.; Li, L.; Frank, L.; Wagner, J.; Andreozzi, P.; Hammer, B.; D'Alicarnasso, M.; Pelliccia, M.; Liu, W.; Chakraborty, S.; Krol, S.; Simon, J.; Landfester, K.; Kuan, S. L.; Stellacci, F.; Müllen, K.; Kreppel, F.; Weil, T. Patchy amphiphilic dendrimers bind

- adenovirus and control its host interactions and in vivo distribution. *ACS Nano* **2019**, *13*, 8749-8759.
17. Litti, L.; Reguera, J.; García de Abajo, F. J.; Meneghetti, M.; Liz-Marzán, L. M. Manipulating chemistry through nanoparticle morphology. *Nanoscale Horiz.*, **2020**, *5*, 102-108.
18. Massart, R. Preparation of aqueous magnetic liquids in alkaline and acidic media. *IEEE transactions on magnetics*, **1981**, *17*, 1247-1248.
19. Daou, T. J.; Pourroy, G.; Bégin-Colin, S.; Grenèche, J. M.; Ulhaq-Bouillet, C.; Legaré, P.; Bernhardt, P.; Leuvre, C.; Rogez, G. Hydrothermal synthesis of monodisperse magnetite nanoparticles. *Chem. Mater.*, **2006**, *18*, 4399-4404.
20. Vijayakumar, R.; Kolytyn, Yu.; Felner, I.; Gedanken, A. Sonochemical synthesis and characterization of pure nanometer-sized Fe<sub>3</sub>O<sub>4</sub> particles. *Mater. Sci. Eng.*, **2000**, *A286*, 101-105.
21. Radziuk, D.; Mikhnavev, L.; Vorokhta, M.; Matolín, V.; Tabulina, L.; Labunov, V. Sonochemical formation of copper/iron-modified graphene oxide nanocomposites for ketorolac delivery. *Chem. Eur. J.*, **2019**, *25*, 6233-6245.
22. Fiadosenka, U.; Matsukovich, A.; Tabulina, L.; Labunov, V.; Radziuk, D. The properties of the sonochemically functionalized nonsteroidal anti-inflammatory drug ketorolac in an Fe<sub>3</sub>O<sub>4</sub>-graphene oxide nanocomposite. *New J Chem.*, **2019**, *41*, 16118-16122.
23. Ma, D.; Chen, J.; Luo, Y.; Wang, H.; Shi, X. Zwitterion-coated ultrasmall iron oxide nanoparticles for enhanced T1-weighted magnetic resonance imaging applications. *J. Mater. Chem. B*, **2017**, *5*, 7267-7273.
24. Lal, M.; Verma, S. R. Synthesis and characterization of polyvinyl alcohol functionalized iron oxide nanoparticles. *Macromol. Symp.*, **2017**, *376*, 1700017.
25. Deng, J.; He, C. L.; Peng, Y.; Wang, J.; Long, X.; Li, P.; Chan, A. S. C. Magnetic and conductive Fe<sub>3</sub>O<sub>4</sub>-PANI nanoparticles with core-shell structure. *Synth. Metals*, **2003**, *139*, 295-301.
26. Jain, T. K.; Morales, M. A.; Sahoo, S. K.; Leslie-Pelecky, D. L.; Labhasetwar, V. Iron oxide nanoparticles for sustained delivery of anticancer agents. *Mol. Pharm.*, **2005**, *2*, 194-205.
27. Rezvantalab, S.; Drude, N. I.; Moraveji, M. K.; Güvener, N.; Koons, E. K.; Shi, Y.; Lammers, T.; Kiessling, F. PLGA-based nanoparticles in cancer treatment. *Front. Pharmacol.*, **2018**, *9*, 1260-1-19.
28. Polymeric nanoparticles as a promising tool for anti-cancer therapeutics. Ed. Kesharwani, P.; Paknikar, K. M.; Gajbhiye, V.; Academic Press Elsevier, 2019, p. 432.
29. Fadeel, B.; Bussy, C.; Merino, S.; Vázquez, E.; Flahaut, E.; Mouchet, F.; Evariste, L.; Gauthier, L.; Koivisto, A. J.; Vogel, U.; Martin, C.; Delogu, L. G.; Bürki-Thurnherr, T.;

- 1  
2  
3 Wick, P.; Beloin-Saint-Pierre, D.; Hischier, R.; Pelin, M.; Carniel, F. C.; Tretiach, M.; Cesca,  
4 F.; Benfenati, F.; Scaini, D.; Ballerini, L.; Kostarelos, K.; Prato, M.; Bianco, A. Safety  
5 assessment of graphene-based materials: focus on human health and the environment. *ACS*  
6 *Nano*, **2018**, *12*, 10582-10620.  
7  
8  
9 30. Martín, C.; Kostarelos, K.; Prato, M.; Bianco, A. Biocompatibility and biodegradability of  
10 2D materials: graphene and beyond. *Chem. Commun.*, **2019**, *55*, 5540-5546.  
11  
12 31. Pinto, A. M.; Moreira, J. A.; Magalhães, F. D.; Gonçalves, I. C.; Gonçalves, I. Polymer  
13 surface adsorption as a strategy to improve the biocompatibility of graphene nanoplatelets.  
14 *Colloid Surf. B.*, **2016**, *146*, 818-824.  
15  
16 32. Marcano, D. C.; Kosynkin, D. V.; Berlin, J. M.; Sinitskii, A.; Sun, Z.; Slesarev, A.; Alemany,  
17 L. B.; Lu, W.; Tour, J. M. Improved synthesis of graphene oxide. *ACS Nano*, **2010**, *4*, 4806-  
18 4814.  
19  
20 33. Edwards, L. J. The dissolution and diffusion of aspirin in aqueous media. *Trans. Faraday*  
21 *Soc.*, **1951**, *47*, 1191-1210.  
22  
23 34. Margulis, M. A.; Margulis, I. M. Calorimetric method for measurement of acoustic power  
24 absorbed in a volume of a liquid. *Ultrason. Sonochem.*, **2003**, *10*, 343-345.  
25  
26 35. Radziuk, D.; Mikhnavev, L.; Tkach, A.; Tabulina, L.; Labunov, V. Sonochemically  
27 assembled photoluminescent copper-modified graphene oxide microspheres. *Langmuir*,  
28 **2018**, *34*, 8599-8610.  
29  
30 36. Zavatski, S.; Khinevich, N.; Girel, K.; Redko, S.; Kovalchuk, N.; Komissarov, I.;  
31 Lukashovich, V.; Semak, I.; Mamatkulov, K.; Vorobyeva, M.; Arzumanyan, G.; Bandarenka,  
32 H. Surface enhanced raman spectroscopy of lactoferrin adsorbed on silvered porous silicon  
33 covered with graphene. *Biosensors*, **2019**, *9*, 34.  
34  
35 37. Cançado, L.; Takai, K.; Enoki, T.; Endo, M.; Kim, Y.A.; Mizusaki, H.; Jorio, A.; Coelho, L.  
36 N.; Magalhães-Paniago, R.; Pimenta, M. A. General equation for the determination of the  
37 crystallite size  $L_a$  of nanographite by Raman spectroscopy. *Appl. Phys. Lett.*, **2006**, *88*,  
38 163106.  
39  
40 38. Ferreira, E. H. M.; Moutinho, M. V. O.; Stavale, F.; Lucchese, M. M.; Capaz, R. B.; Achete,  
41 C. A.; Jorio, A. Evolution of the Raman spectra from single-, few-, and many-layer graphene  
42 with increasing disorder. *Phys. Rev. B*, **2010**, *82*, 125429.  
43  
44 39. Ferrari, A. C.; Robertson, J. Interpretation of Raman spectra of disordered and amorphous  
45 carbon. *Phys. Rev. B*, **2000**, *61*, 14095-14107.  
46  
47 40. Ferrari, A. C. Raman spectroscopy of graphene and graphite: Disorder, electron-phonon  
48 coupling, doping and nonadiabatic effects. *Solid State Commun.*, **2007**, *143*, 47-57.  
49  
50 41. Nakamoto, K. Infrared and Raman spectra of inorganic and coordination compounds. 4<sup>th</sup> Ed.  
51 John Wiley & Sons, 1984, p. 484.  
52  
53  
54  
55  
56  
57  
58  
59  
60

- 1  
2  
3  
4 42. Khandelwal, M.; Kumar, A. One-step chemically controlled wet synthesis of graphene  
5 nanoribbons from graphene oxide for high performance supercapacitor applications. *J.*  
6 *Mater. Chem. A*, **2015**, *3*, 22975-22988.
- 8 43. Lia, Y.-S.; Church, J. S.; Woodhead, A. L. Infrared and Raman spectroscopic studies on iron  
9 oxide magnetic nano-particles and their surface modifications. *J. Magn. Magn. Mater.*, **2012**,  
10 *324*, 1543-1550.
- 12 44. de Faria, D. L. A.; Silva, S. V.; de Oliveira, M. T.; Raman microspectroscopy of some iron  
13 oxides and oxyhydroxides. *J Raman Spectrosc.*, **1997**, *28*, 873-878.
- 15 45. Trusovas, R.; Račiukaitis, G.; Niaura, G.; Barkauskas, J.; Valušis, G.; Pauliukaite, R. Recent  
16 advances in laser utilization in the chemical modification of graphene oxide and its  
17 Applications. *Adv. Optical Mater.*, **2016**, *4*, 37-65.
- 19 46. Soler, M. A. G.; Qu, F. Chapter 14: Raman spectroscopy of iron oxide nanoparticles. Challa  
20 S. S. R. Kumar (ed.), Raman spectroscopy for nanomaterials characterization, Springer-  
21 Verlag Berlin Heidelberg 2012, 379-416.
- 23 47. Perkins, R. S.; Garber, J. D. Raman spectroscopy of iron in aqueous carbonate solutions. *J*  
24 *Sol. Chem.*, **2003**, *32*, 265-272.
- 26 48. Ferrari, A. C.; Robertson, J. Origin of the 1150 cm<sup>-1</sup> Raman mode in nanocrystalline  
27 diamond. *Phys. Rev. B*, **2001**, *63*, 121405-1-4.
- 29 49. Díez-Betriu, X.; Álvarez-García, S.; Botas, C.; Álvarez, P.; Sánchez-Marcos, J.; Prieto, C.;  
30 Menéndez, R.; de Andrés, A. Raman spectroscopy for the study of reduction mechanisms  
31 and optimization of conductivity in graphene oxide thin films. *J. Mater. Chem. C*, **2013**, *1*,  
32 6905-6912.
- 34 50. Wang, Y.; Alsmeyer, D. C.; McCreery, R. L. Raman spectroscopy of carbon materials:  
35 structural basis of observed spectra. *Chem. Mater.*, **1990**, *2*, 557-563.
- 37 51. Loh, K. P.; Bao, Q.; Eda, G.; Chhowalla, M. Graphene oxide as a chemically tunable  
38 platform for optical applications. *Nat. Chem.*, **2010**, *2*, 1015-1024.
- 40 52. Guo, P.; Song, H.; Chen, X. Hollow graphene oxide spheres self-assembled by W/O  
41 emulsion. *J. Mater. Chem.*, **2010**, *20*, 4867-4874.
- 43 53. Krishnamoorthy, K.; Veerapandian, M.; Yun, K.; Kim, S.-J. The chemical and structural  
44 analysis of graphene oxide with different degrees of oxidation. *Carbon*, **2013**, *53*, 38-49.
- 46 54. Suslick, K. S.; Hammerton, D. A.; Cline, R. E. The sonochemical hot spot. *J. Am. Chem.*  
47 *Soc.*, **1986**, *108*, 5641-5642.
- 49 55. Lavina, B.; Dera, P.; Kim, E.; Meng, Y.; Downs, R. T.; Weck, P. F.; Sutton, S. R.; Zhao, Y.  
50 Discovery of the recoverable high-pressure iron oxide Fe<sub>4</sub>O<sub>5</sub>. *PNAS*, **2011**, *108*, 17281-  
51 17285.
- 53  
54  
55  
56  
57  
58  
59  
60

- 1  
2  
3  
4 56. Tang, L.; Ji, R.; Cao, X.; Lin, J.; Jiang, H.; Li, X.; Teng, K. S.; Luk, C. M.; Zeng, S.; Hao, J.;  
5 Lau, S. P. Deep ultraviolet photoluminescence of water-soluble self-passivated graphene  
6 quantum dots. *ACS Nano*, **2012**, *6*, 5102-5110.  
7  
8 57. Liang, Y.; Wu, D.; Feng, X.; Müllen, K. Dispersion of graphene sheets in organic solvent  
9 supported by ionic interactions. *Adv. Mater.*, **2009**, *21*, 1679-1683.  
10  
11 58. He, Y. P.; Miao, Y. M.; Li, C. R.; Wang, S. Q.; Cao, L.; Xie, S. S.; Yang, G. Z.; Zou, B. S.;  
12 Burda, C. Size and structure effect on optical transitions of iron oxide nanocrystals. *Phys.*  
13 *Rev. B*, **2005**, *71*, 125411.  
14  
15 59. Rainsford, K. D. Aspirin and related drugs, CRC Press Inc., UK, 2004, p. 800.  
16  
17 60. Lai, Q.; Zhu, S.; Luo, X.; Zou, M.; Huang, S. Ultraviolet-visible spectroscopy of graphene  
18 oxides. *AIP Advances*, **2012**, *2*, 032146.  
19  
20 61. Robinson, J. W. Practical handbook of spectroscopy, Section 7, p. 578, CRC Press Inc., UK,  
21 1991.  
22  
23 62. Tang, J.; Myers, M.; Bosnick, K. A.; Brus, L. E. Magnetite Fe<sub>3</sub>O<sub>4</sub> nanocrystals:  
24 spectroscopic observation of aqueous oxidation kinetics. *J. Phys. Chem. B*, **2003**, *107*, 7501-  
25 7506.  
26  
27 63. Brela, M. Z.; Wójcik, M. J.; Witek, Ł. J.; Boczar, M.; Wrona, E.; Hashim, R.; Ozaki, Y.  
28 Born–Oppenheimer molecular dynamics study on proton dynamics of strong hydrogen bonds  
29 in aspirin crystals, with emphasis on differences between two crystal forms. *J Phys. Chem. B*,  
30 **2016**, *120*, 3854-3862.  
31  
32 64. Berg, R. W. Investigation of L(+)-ascorbic acid with Raman spectroscopy in visible and UV  
33 light. *Appl. Spectrosc. Rev.*, **2015**, *50*, 193-239.  
34  
35 65. Boczar, M.; Wójcik, M. J.; Szczeponek, K.; Jamróz, D.; Zięba, A.; Kawalek, B. Theoretical  
36 modeling of infrared spectra of aspirin and its deuterated derivative. *Chem. Phys.*, **2003**, *286*,  
37 63-79.  
38  
39 66. Cooney, T. F.; Wang, L.; Sharma, S. K.; Gauldie, R. W.; Montana, A. J. Raman spectral  
40 study of solid and dissolved poly(vinyl alcohol) and ethylene-vinyl alcohol copolymer. *J*  
41 *Polym. Sci.: Part B: Polym. Phys.*, **1994**, *32*, 1163-1174.  
42  
43  
44  
45  
46  
47  
48  
49  
50  
51  
52  
53  
54  
55  
56  
57  
58  
59  
60



## Table of Contents Graphic

Coating of ultrasonically formed acetylsalicylic acid- $\text{Fe}_3\text{O}_4$ -graphene oxide nanocomposites with polyvinyl alcohol substantially enhances acetylation of pristine ascorbic acid.

